Rational Design of Polymeric Hybrid Micelles with Highly Tunable Properties to Co-Deliver MicroRNA-34a and Vismodegib for Melanoma Therapy

*Hanmei Li, Yao Fu, Ting Zhang, Yanping Li, Xiaoyu Hong, Jiayu Jiang, Tao Gong, Zhirong Zhang, and Xun Sun**

A polymeric hybrid micelle (PHM) system with highly tunable properties is reported to co-deliver small molecule and nucleic acid drugs for cancer therapy; this system is structurally simple and easy-to-fabricate. The PHM consists of two amphiphilic diblock copolymers, polycaprolactone-polyethylenimine (PCL-PEI) and polycaprolactone-polyethyleneglycol (PCL-PEG). PHMs are rationally designed with different physicochemical properties by simply adjusting the ratio of the two diblock copolymers and the near neutral PHM-2 containing a low ratio of PCL-PEI achieves the optimal balance between high tumor distribution and subsequent cellular uptake after intravenous injection. Encapsulating Hedgehog (Hh) pathway inhibitor vismodegib (VIS) and microRNA-34a (miR-34a) into PHM-2 generates the VIS/PHM-2/34a co-delivery system. VIS/PHM-2/34a shows synergistic anticancer efficacy in murine B16F10-CD44$^+$ cells, a highly metastatic tumor model of melanoma. VIS/PHM-2/34a synergistically attenuates the expression of CD44, a vital receptor indicating the metastasis of melanoma. Intriguingly, inhibiting Hh pathway by VIS is accompanied by downregulation of CD44 expression, revealing that Hh signaling might be an upstream regulator of CD44 expression in melanoma. Thus, co-delivery of miR-34a and VIS demonstrates great potential in cancer therapy, and PHM offers a structurally simple and highly tunable platform for the co-delivery of small molecule and nucleic acid drugs in tumor combination therapy.

1. Introduction

In recent years, nucleic acid therapeutics such as microRNAs (miRNAs), small interfering RNA, and plasmid DNA have shown great promise in cancer treatment.[1] Cancers are complex diseases involving multiple signaling pathways, and their progression is marked by many successive mutations in a line of cells.[2] Inhibition of one signaling pathway by a single drug may be insufficient for sustained and complete tumor response. Therefore, nucleic acid-based anticancer therapies are currently under intense investigation in combination with small molecule anticancer drugs, with the goal of improving the therapeutic outcome of cancer treatment.[3]

For the drug–nucleic acid combination chemotherapy, appropriate nanocarriers are needed to avoid nucleic acid degradation in the circulation, and deliver drug–nucleic acid combinations to cancer cells in a synchronized fashion to achieve synergistic antitumor effects.[4] Recently, the cationic block polymeric nanocarriers comprised with hydrophobic and cationic hydrophilic segments have become promising carriers for co-delivery of drug–nucleic acid combinations.[5] Due to the drastic differences in their physicochemical properties between the nucleic acid and small molecule drugs, separate mechanisms are usually required to encapsulate these two distinct drug types. Hydrophobic small molecule drugs can be encapsulated within the hydrophobic core of polymeric nanocarriers via hydrophobic interaction, while a dominant approach for encapsulating nucleic acids drug is to employ cationic hydrophilic segments. The cationic moieties in the polymeric nanocarriers serve several functions: (i) to form polyplexes with the negatively charged nucleotides and protect them against nuclease degradation; (ii) to facilitate the interaction with the cell membrane and promote the intracellular uptake of the nanocarriers via endocytosis; and (iii) to aid in endosomal escape of the nucleic acids.

The proportion of cationic segments in polymeric nanocarriers is a structural parameter of crucial importance.[6] Adequate proportion of cationic segments is required to ensure the complexation of nucleic acid drug and promote adequate levels of intracellular delivery.[7] However, high proportion of cationic segments has also been shown to correlate with short circulation time in the bloodstream and high toxicity. Therefore, the proportion of cationic block needs to be systematically studied and tailored to afford the polymeric nanocarriers with optimal co-delivery performance. Unfortunately, for the polymeric nanocarriers, it is complicated to regulate the proportion

H. Li, Dr. Y. Fu, T. Zhang, Dr. Y. Li, X. Hong, J. Jiang, Prof. T. Gong, Prof. Z. Zhang, Prof. X. Sun
Key Laboratory of Drug Targeting and Drug Delivery Systems
Ministry of Education
West China School of Pharmacy
Sichuan University
Chengdu 610041, P.R. China
E-mail: sunxun@scu.edu.cn

DOI: 10.1002/adfm.201503115

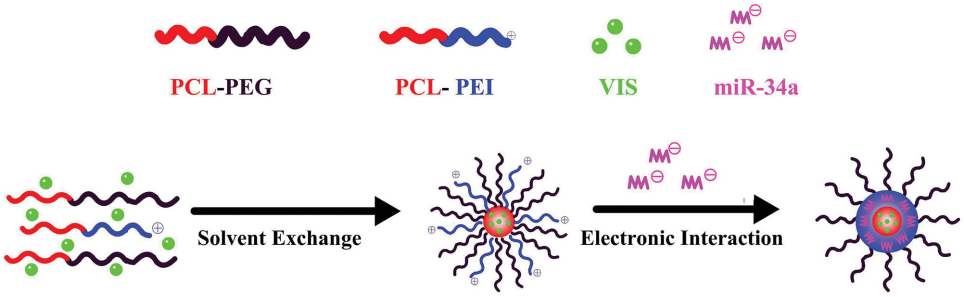

Scheme 1. PHM self-assembly and loading with miR-34a and VIS.

of cationic segments.[8] The copolymer materials usually require extensive and time-consuming synthesis to alter their architecture. Thus, there is an urgent need for a highly versatile polymeric nanocarrier, whose structural features especially the proportion of cationic segments can be easily tailored.

Polymeric hybrid micelles (PHMs), consisting of different amphiphilic diblock copolymers, provide an exciting new class of drug delivery platforms with promising clinical translational potential.[9] The PHM system allows much easier optimization of physicochemical properties than the conventional polymeric nanocarriers. Simply adjusting the ratio of the two diblock copolymers instead of altering the copolymer architecture allows easy regulations of the proportion of cationic segments in PHMs. Therefore, the use of PHMs is a new and highly promising approach enabling the generation of highly versatile polymeric nanocarrier for co-delivery. However, PHMs have been designed mostly for single drug delivery in the past 2–3 years,[10] and the co-delivery of small molecule and nucleic acid drugs using PHMs remains largely unexplored. Herein, we investigate the potential of PHMs for co-loading of small molecule and nucleic acid drugs. Hedgehog (Hh) pathway inhibitor vismodegib (VIS) and microRNA-34a (miR-34a) were used as model drugs. For the first time, we designed a PHM system consisting of two amphiphilic diblock copolymers, polycaprolactone-polyethylenimine (PCL-PEI) and polycaprolactone-polyethyleneglycol (PCL-PEG), for the co-delivery of small molecule and nucleic acid drugs.

Another important goal of the study is to investigate the correlation between the physicochemical properties of PHMs and their interactions with biological systems. Researchers have been focused on the synthesis of novel materials to fabricate PHMs for anticancer drug delivery.[11] However, poor understanding of the correlation between the physicochemical properties of PHMs and their interactions with biological systems has significantly hindered their anticancer efficacy. To achieve superior anticancer activities, it is essential to investigate this correlation to establish principles for the rational design of PHMs. Unfortunately, detailed structure–function relationships for PHM have been rarely reported. In the current studies, various PHMs were formulated with different ratios of PCL-PEI and PCL-PEG to enable a systematic study of the relationship between physicochemical properties of PHMs and their interactions with biological systems.

Herein, PHMs with different ratios of PCL-PEI and PCL-PEG were characterized in vitro for stability, hemocompatibility, cytotoxicity, and intracellular delivery and in vivo for tissue biodistribution and systemic toxicities. Then the miR-34a and VIS were co-encapsulated into the optimal PHM system (**Scheme 1**). The physicochemical properties of this dual drug co-delivery system were characterized, and its anticancer efficacy against a highly metastatic melanoma cell line B16F10-$CD44^+$ was assessed both in vitro and in vivo.

2. Results and Discussions

2.1. Tuning Properties of PHMs to Overcome Intracellular and Systemic Delivery Barriers

Our PHMs are prepared from the self-assembly of two amphiphilic diblock copolymers, PCL-PEI and PCL-PEG, into a stable cationic micelle. Both PCL-PEI and PCL-PEG possess hydrophobic blocks of biocompatible poly-(caprolactone) (PCL), but differ in hydrophilic blocks, with PCL-PEI possessing the PEI block which is partially protonated under physiological conditions, and PCL-PEG possessing the hydrophilic block of PEG. The partially protonated amine groups in PEI block will complex nucleic acid drug and possess sufficient buffering capacity to promote endosomal rupture through the "proton sponge effect," facilitating endosomal escape into the cell.[7a,12] The hydrophobic block PCL could compose the inner core of PHMs and efficiently encapsulate the hydrophobic drugs. The function of PEG block is to provide colloidal stability to the micelle, thus increasing its in vivo circulation time.

To fabricate PHMs, PCL-PEI and PCL-PEG were firstly synthesized by conjugating, branched poly-(ethyleneimine) (M_W = 2000, PEI_{2k}) or primary amine-terminated polyethyleneglycol (M_W = 5000, $mPEG_{5k}$-NH_2) with 4-nitrophenyl chloroformate-activated PCL (PCL-NPC) (Scheme S1, Supporting Information). The molecular weight of PCL-PEG and PCL-PEI was 8400 and 4900 Da, respectively, based on gel permeation chromatography. The confirmation of chemical structure and critical micelle concentration of PCL-PEG and PCL-PEI are shown in Figures S1–S3 (Supporting Information).

To investigate how the proportion of cationic segments affects the properties of PHMs, we prepared PHMs with different weight ratios of PCL-PEI ranging from 0% (PHM-0) to 100% (PHM-100). As the weight ratio of PCL-PEI decreased from 100% (PHM-100) to 2% (PHM-2), the size of PHM was in the same range (**Figure 1**A), while zeta potential decreased from +43.5 to +4.32 mV (Figure 1B). As expected, the net cationic charge of PHMs can be modulated simply by changing the

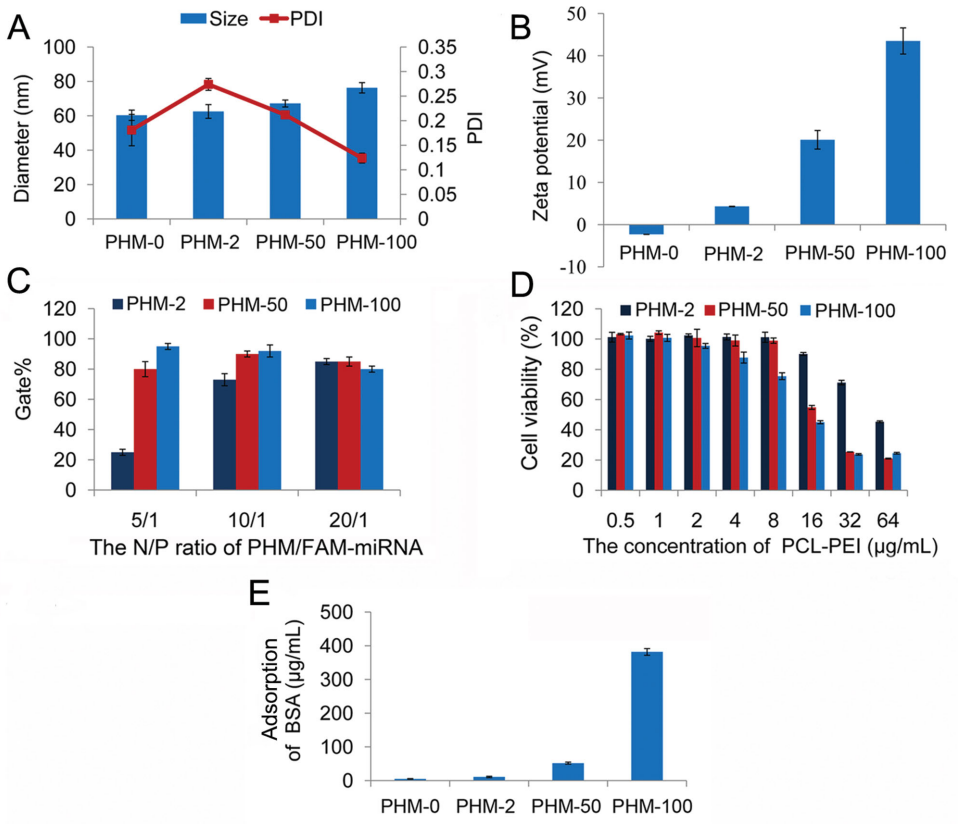

Figure 1. In vitro characterization of PHMs and PHM/miRNA complexes. A) Hydrodynamic size and polydispersity index (PDI) of PHMs containing variable ratios of PCL-PEI and PCL-PEG ($n = 3$, mean ± SD). B) Zeta-potential of PHMs containing variable ratios of PCL-PEI and PCL-PEG ($n = 3$, mean ± SD). C) Uptake by B16F10-CD44$^+$ cells of PHMs prepared with different loading ratios of FITC-miRNA ($n = 3$, mean ± SD). Cells were treated for 4 h with PHM/FITC-miRNA complexes at N:P ratios of 5:1, 10:1, and 20:1, and cellular uptake was measured by flow cytometry. D) Cytotoxicity of PHMs prepared with various concentrations of PCL-PEI in B16F10-CD44$^+$ cells after 24 h incubation ($n = 6$, mean ± SD). E) Stability of PHMs in bovine serum albumin (BSA) after incubation for 4 h at 37 °C. The amount of BSA adsorbed by PHMs was determined by centrifuging the mixtures and analyzing the supernatant with a BSA assay kit ($n = 3$, mean ± SD).

molar ratios of PCL-PEI:PCL-PEG. This PHM approach avoids the need for extensively and time-consuming resynthesis of copolymer materials to adjust the properties of polymeric nanocarriers. Unlike single diblock copolymers or triblock copolymers, the two independent amphiphilic diblock copolymers open the possibility of constructing rapidly numerous polymeric nanocarrier compositions.

A desirable cationic gene carrier must possess the capacity of condensing genes efficiently. The cationic charges of PCL-PEI in PHMs play a critical role in condensing negatively charged nucleic acid drugs. Thus, it is necessary to assess the gene condensation ability of PHMs with varying cationic charge. As shown in the gel retardation assay, PHM-2, PHM-50, and PHM-100 were able to complex with miRNA in a dose-dependent manner, with no free miRNA detectable at an N:P ratio of 8:1 (Figure S4, Supporting Information), indicating all PHMs can efficiently condense miRNA. Based on the results of gel retardation assay, the gene delivery ability of different PHM formulations was investigated by examining the uptake of PHM/FAM-labeled miRNA complex by cultures of B16F10-CD44$^+$ melanoma cells after 4 h incubation. Flow cytometry analysis showed that cellular uptake increased with increasing N:P ratio (Figure 2C). Increasing the amount of PCL-PEG in the PHMs sharply reduced cellular uptake at an N:P ratio of 5:1, but reduced it only slightly at ratios of 10:1 and 20:1. Importantly, similarly high cellular uptake was observed with PHM-2, PHM-50, and PHM-100 at N:P ratios of 10:1 and 20:1. These results indicate that although PHM-2 contains very low proportions of PCL-PEI, it can efficiently condense and deliver miRNA. More importantly, the cytotoxicity of PHMs on B16F10-CD44$^+$ melanoma cells showed PHM-2 was associated with the highest cell viability than any of the other PHMs at all the PCL-PEI concentration (Figure 1D). The high proportion of PCL-PEG in PHM-2 can efficiently prevent the cationic PCL-PEI from interrupting with the cell membrane, which rendered PHM-2 an efficient and low toxic gene carrier.

Upon intravenous injection, cationic polymeric nanocarriers are prone to aggregate due to interactions with high abundance of serum proteins and red blood cells, which may further affect the distribution and pharmacokinetics of delivery therapeutics and cause toxicity due to emboli within lung capillaries.[7b,8c,9b] To predict in vivo translatability based on ability to overcome systemic delivery barriers, we used the bovine serum albumin (BSA) adsorption assay to investigate the stability of PHM. The results showed that the amount of BSA adsorbed by PHMs decreased with increasing proportion of PCL-PEG (Figure 1E), suggesting

that of all PHM formulations, PHM-2 was the most stable in blood and would be the most compatible for in vivo studies. PHM-2 with high proportion of PCL-PEG, surrounded by a thick PEG shell, had decreased z-potential and charge density, thus resulting in increased colloidal stability and reduced cytotoxicity.

To assess the influence of PCL-PEG and PCL-PEI on the delivery efficacy of PHMs in vivo, the biodistribution of PHMs loaded with Cy5-miRNA after injection intravenously into mice bearing B16F10-CD44$^+$ melanoma xenografts was investigated using near-infrared fluorescence imaging (Figure S5, Supporting Information). Fluorescent imaging demonstrated that a large percentage of the PHMs accumulated in the liver for PHM-50 and PHM-100. In addition, the PHM-100 resulted in much higher fluorescence in the lungs compared to PHM-50. The higher lung accumulation of the PHM-100 may be due to lodging of aggregates within lung capillaries, consistent with the ex vivo BSA adsorption assay data in Figure 1E. Of all PHM formulations, PHM-2 showed the least aggregation within the lungs and the liver, as well as the greatest aggregation in the tumor. After intravenous injection, the higher positively charged PHM-100 (containing 100% of PCL-PEI) interacted with blood plasma proteins and erythrocytes immediately, causing the formation of aggregates which could be trapped in lung capillaries and cleared by reticuloendothelial system. Consequently, PHM-100 fast cleared from the circulation and distributed mainly in the lungs and liver. Mixing PCL-PEI with PCL-PEG formed the less positively charged PHMs such as PHM-50 and PHM-2. PCL-PEG could form a sterically stabilizing PEG layer on the nanoparticle surface to prevent particle aggregation, enhance their colloidal stability in the presence of serum protein and thus potentially extend blood circulation, increase tumor targeting by the enhanced permeability and retention (EPR) effect. The more PCL-PEG PHMs contains, the denser PEG layer coated on the nanocarriers, which lead to higher distribution into the tumor and less accumulation in the liver and lungs. Besides, these data also imply that simply altering the ratios of PCL-PEG:PCL-PEI can modulate in vivo half-life and biodistribution of PHMs.

To evaluate the safety of PHMs, the hemolytic activity of PHMs was investigated firstly.[13] Hemolytic activity decreased with decreasing amount of PCL-PEI (Figure S6, Supporting Information). PHM-2 showed the comparable hemolytic activity to that of PHM-0. Afterward, the pulmonary toxicity and immunogenicity of PHMs were investigated in C57BL/6 mice. Animals injected with PHM-100 exhibited severe pulmonary inflammation due to the presence of neutrophils, as well as extensive alveolar rupture and lung tissue collapse. This toxicity is the result of cationic PHMs nonspecifically interacting with blood plasma proteins and erythrocytes, causing the formation of aggregates that can occlude the pulmonary vasculature.[1c,13,14] At the other extreme, animals injected with PHM-2 showed pulmonary histology similar to that of the control group (Figure S7, Supporting Information). Induction of immune response as measured by serum levels of the proinflammatory cytokine IL-12 decreased with increasing amount of PCL-PEG (Figure S8, Supporting Information). Serum IL-12 levels were similar in animals treated with PHM-2 or saline. This probably reflects the nearly neutral surface charge of PHM-2 and the high shielding ability of PCL-PEG.

Taken together, these initial studies demonstrated that while cationic PHMs with high surface charge (PHM-100 and PHM-50) could produce satisfactory intracellular delivery ability in vitro, they showed poor hemocompatibility upon intravenous injection in vivo, leading to fast elimination in circulation and unexpected toxicity. The near neutral PHMs containing very low proportion of PEI-PCL (such as PHM-2) could also deliver the nucleic acids to the tumor cells with high efficiency. More importantly, the PHM-2 is also ideally suitable to overcome systemic biological barriers, showing excellent stability in circulation and tumor targeting ability via EPR effect. Based on these studies, we select PHM-2 with the highest proportion of PCL-PEG as the candidate delivery vehicle associated with excellent delivery performance and minimal toxicity. Therefore all further experiments were carried out with PHM-2.

2.2. Preparation and Physicochemical Characterization of miR-34a/VIS-Loaded PHM-2

MiR-34a is one of the most well-defined tumor suppressor miRNAs in a variety of tumors. In 2013, a miR-34 mimic has become the first miRNA to reach phase I clinical trials, indicated that miR-34a-based therapy has great potential in cancer treatment.[1b] Overexpression of miR-34a in melanoma cells induces cell apoptosis and inhibits cell migration and tumor growth in vivo.[15] VIS was a Hh pathway inhibitor approved in 2012 for the treatment of basal cell carcinoma. A recent study showed that VIS could inhibit melanoma growth in vitro and in vivo.[16] In the present study, miR-34a and VIS were co-encapsulated into PHMs to investigate their synergistic effects in melanoma suppression. To our knowledge, this is the first example of co-delivery of miRNAs and Hh pathway inhibitor for cancer therapy.

VIS was first encapsulated into PHM-2 to obtain VIS/PHM-2, which was incubated with miR-34a at an N:P ratio of 10:1 to yield VIS/PHM-2/34a. VIS/PHM-2 and VIS/PHM-2/34a micelles showed a similar average size of about 65 nm by dynamic light scattering. Consistent with this result, both formulations appeared as compact spheres with a diameter around 70 nm by transmission electron microscopy (Figure S9, Supporting Information). In addition, the polydispersity index (PDI) of these PHM-2, VIS/PHM-2, and VIS/PHM-2/34a was 0.253, 0.275, and 0.194, respectively, indicating narrow size distribution of the obtained nanoparticle. The zeta-potential of VIS/PHM-2 and VIS/PHM-2/34a was +4.54 and +3.42 mV, respectively, reflecting the nearly neutral surface charge of drug-loaded PHM-2. Detailed characterization studies revealed that VIS and miRNA were incorporated into the PHM-2 with extraordinarily high encapsulation efficiencies of 97.6% and 95.3%, respectively. The drug loading capacity of VIS and miR-34a was 2% and 0.13%, respectively.

Besides, VIS showed sustained drug release from VIS/PHM-2 lasting up to 24 h (**Figure 2**A). In the initial 4 h, the cumulative release percentage of free VIS reached 95%, while it was less than 60% for VIS/PHM-2. VIS/PHM-2/34a and VIS/PHM-2 showed similar VIS release profiles, indicating that the presence of miR-34a did not significantly affect VIS release. Differential thermal analysis (DTA) showed a decomposition

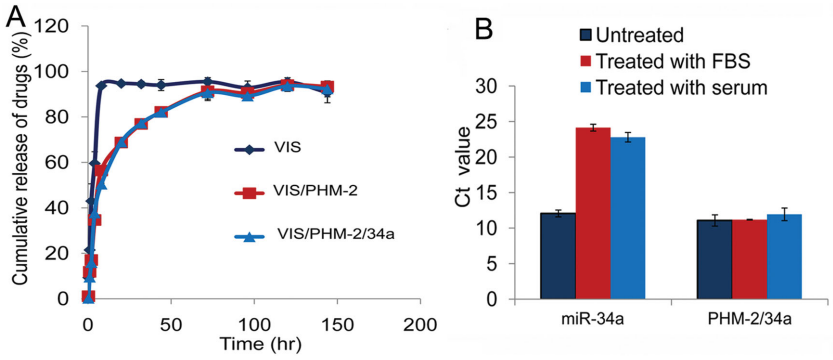

Figure 2. Characterization of VIS/PHM-2/34a. A) Profiles of VIS release from VIS/PHM-2 and VIS/PHM-2/34a in PBS containing 0.2% Tween 80 ($n = 3$, mean ± SD). B) Stability of miR-34a, measured in terms of threshold cycle (C_t) values using real-time PCR, after incubation in serum from C57BL/6 mice or FBS for 6 h ($n = 3$, mean ± SD).

peak at 178 °C for unencapsulated VIS (Figure S10, Supporting Information), consistent with its reported melting point.[17] No such peak was observed for VIS/PHM-2, suggesting that VIS was encapsulated in the inner core of PHM-2.

To assess whether miR-34a encapsulated within VIS/PHM-2/34a is likely to be protected from nuclease degradation in vivo, we examined the stability of the miRNA in serum from C57BL/6 mice and in 5% fetal bovine serum (FBS). Stability was measured in terms of threshold cycle (C_t) value using quantitative real-time polymerase chain reaction (PCR), with higher C_t values indicating smaller amounts of residual miR-34a (Figure 2B). C_t values for miR-34a in VIS/PHM-2/34a were 11.2 and 11.9 after incubating in serum or FBS for 6 h, similar to the C_t value for free miR-34a not exposed to FBS or serum. These values were much smaller than those for unencapsulated miR-34a after incubation in FBS (24.1) or serum (22.8). These results suggest that VIS/PHM-2/34a can efficiently protect miR-34a from degradation in the presence of serum.

2.3. PHM-2 Co-deliver VIS and miR-34a into B16F10-CD44$^+$ Cells

Uptake of VIS/PHM-2/34a into B16F10-CD44$^+$ cells in culture and release of both cargoes into the cytoplasm were evaluated by confocal microscopy. To allow separate detection of VIS and miR-34a, the VIS was replaced by fluorescent molecule 1,1-dioctadecyl-3,3,3′,3′-tetramethyl indodicarbocyanine, 4-chlorobenzenesulfonate salt (DiD), while the miR-34a was replaced with FITC-miRNA. The resulting PHM-2 micelles were designated DiD/PHM-2/FITC-miRNA. After incubating these micelles with B16F10-CD44$^+$ cells for 4 h, DiD and FITC-miRNA fluorescence was observed primarily in the cytoplasm (**Figure 3**A). These results indicate that VIS/PHM-2/34a can simultaneously deliver both therapeutic agents into the cytosol of melanoma cells.

After internalization via endocytosis, VIS/PHM-2/34a should escape from the endosome/lysosome and release miR-34a into the cytoplasm. To examine the internalization and subcellular localization of VIS/PHM-2/34a in B16F10-CD44$^+$ cells in greater detail, we co-tracked the green fluorescence of FITC-miRNA in VIS/PHM-2/FITC-miRNA and the red fluorescence of Lyso-Tracker, which labels endosomes and lysosomes, respectively. Extensive co-localization of FITC-miRNA with endosome/lysosome (visible as yellow fluorescence) was observed 1 h after micelles were added to cells (Figure 3B). After 4 h, most green fluorescence was observed in the cytosol, with much less overlap with red fluorescence. These results indicated that VIS/PHM-2/34a was efficiently taken up into the endosome/lysosomal compartments, after which the cargo enters the cytosol.

To explore how VIS/PHM-2/34a is internalized into B16F10-CD44$^+$ cells, we repeated cell uptake experiments with VIS/PHM-2/FITC-miRNA at 4 °C or in the presence of various endocytosis inhibitors. Uptake was decreased markedly by incubation at 4 °C or treatment with chlorpromazine (Figure 3C), suggesting that PHM-2 micelles should be internalized primarily by a clathrin-mediated, energy-dependent process.

To provide definitive quantitation of VIS and miR-34a taken up by B16F10-CD44$^+$ cells, we performed uptake experiments using liquid chromatography-mass spectrometry (LC-MS) to measure internalized VIS and real-time PCR to measure internalized miRNA. Cells took up substantially more VIS when they were exposed to VIS/PHM-2 (4.35 ng mL^{-1}) or VIS/PHM-2/34a (4.15 ng mL^{-1}) than when they were exposed to unencapsulated VIS (0.96 ng mL^{-1}; Figure 3D). Similar results were obtained for miR-34a (Figure 3E). These results suggest that PHM-2 can significantly enhance uptake of VIS and miR-34a into melanoma cells. These results also suggest that the encapsulation of VIS or the absorption of negative miR-34a does not significantly affect cellular uptake of either two drug by B16F10-CD44$^+$ cells.

2.4. VIS/PHM-2/34a Efficiently Inhibits Cell Proliferation and Promotes Apoptosis In Vitro

To investigate whether the PHM-mediated intracellular co-delivery of miR-34a and VIS can effectively increase the chemotherapeutic efficacy of VIS, proliferation of B16F10-CD44$^+$cells treated with PHM-2 in different formulations was evaluated by cell counting kit-8 (CCK-8) assay. No obvious cell death was noticed in cells treated with blank PHM-2, indicating the low cytotoxicity of PHM-2 (**Figure 4**A). Exposing cells to either encapsulated drug (VIS/PHM-2 or PHM-2/34a) led to substantially lower cell viability than exposing them to either unencapsulated drug (VIS or miR-34a). This is consistent with uptake experiments showing that PHM-2 enhances the amount of internalized miR-34a or VIS. Significant decreases in cell viability were observed in the cell samples treated with VIS/PHM-2/34a compared to those treated with VIS/PHM-2, suggesting that VIS/PHM-2/34a has an increased cytotoxic activity to B16F10-CD44$^+$ cells than VIS/PHM-2 and the increase in cytotoxic activity of VIS/PHM-2/34a is mediated by the additional co-incorporation

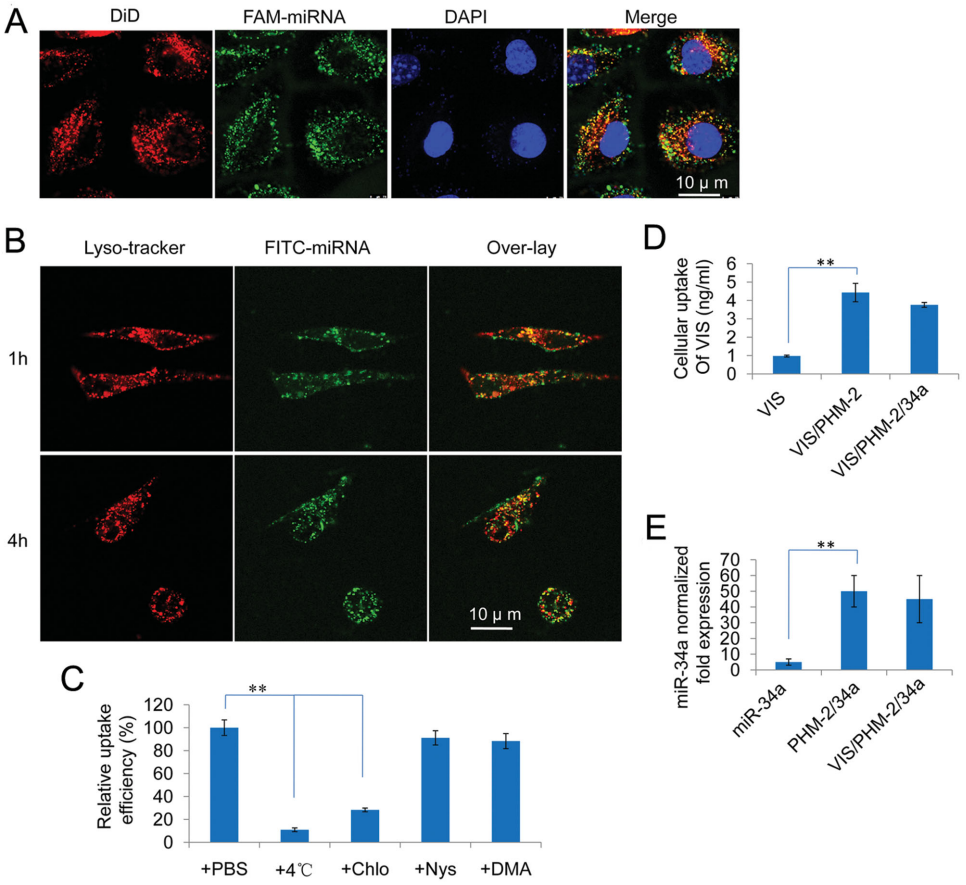

Figure 3. Uptake of VIS/PHM-2/34a by B16F10-CD44$^+$ cells. A) Confocal micrographs of B16F10-CD44$^+$ cells incubated for 4 h at 37 °C with DiD/PHM-2/FITC-miRNA. Bar, 10 μm. B) Confocal micrographs showing escape of PHM-2/FITC-miRNA from the endosome/lysosome. B16F10-CD44$^+$ cells were incubated with PHM-2/FITC-miRNA for 1or 4 h and then stained with Lyso-Tracker. Bar, 10 μm. C) Effect of reduced temperature (4 °C) and endocytic inhibitors on uptake of PHM-2/FITC-miRNA by B16F10-CD44$^+$ cells ($n = 3$, mean ± SD). $^{**}p < 0.01$. D,E) Quantitation of VIS and miR-34a uptake by B16F10-CD44$^+$ cells ($n = 3$, mean ± SD). $^{**}p < 0.01$.

of miR-34a. In our experiments, the combination treatment exhibited greater inhibition on cell proliferation than the individual treatments using either miR-34a or VIS.

We thereafter investigated whether synergistic effects of miR-34a and VIS in cytotoxicity were mediated by increased apoptosis induced by PHM-mediated intracellular delivery of miR-34a and VIS. Changes in nuclear morphology were examined by light microscopy after 4′ 6-diamidino-2-phenylindole (DAPI) staining. Nuclei of normal cells appear bright blue and show homogeneous chromatin, while nuclei of apoptotic cells show such changes as chromatin fragmentation, nuclear condensation, and formation of apoptotic bodies.[18] Cells treated with VIS/PHM-2/34a, VIS/PHM-2, or PHM-2/34a showed significantly more nuclear changes than control cells (Figure S11, Supporting Information), with VIS/PHM-2/34a causing more changes than the other two PHM formulations. These qualitative findings were confirmed by determining the percentage of apoptotic cells under each condition based on double staining with propidium iodide (PI) and FITC-annexin V, followed by flow cytometry. The proportion of apoptotic cells was 46% for VIS/PHM-2/34a, 31.3% for VIS/PHM-2, and 25.9% for PHM-2/34a (Figure 4B,C). The highest percentage of cell apoptosis was obtained in cells treated with VIS/PHM-2/34a, suggesting that miR-34a and VIS have synergistic effects on cell apoptosis and the co-delivery of miR-34 with VIS enhances VIS-mediated cell apoptosis, which in turn increases chemotherapeutic efficacy of VIS.

2.5. VIS/PHM-2/34a Inhibits Migration and Invasion of B16F10-CD44$^+$ Cells

In melanoma, metastasis-related recurrence is still common and responsible for the majority of melanoma-associated mortality.[19] Inhibition of migration and invasion has been thus emerging as an effective strategy for melanoma treatment by preventing tumor metastasis. We were therefore interested in investigating the regulatory effects of VIS/PHM-2/34a on migration and invasion of B16F10-CD44$^+$ cells. Cells treated with VIS/PHM-2 showed only 28% of the invasion seen with control cells; cells treated with PHM-2/34a, 37%; and cells treated with VIS/PHM-2/34a, only 10% (Figure 4D,E). In migration assays, cultures were incubated with phosphate-buffered saline (PBS), unencapsulated VIS, or PHM-2 micelles, then scratched and analyzed 72 h later. Cultures preincubated with PBS or unencapsulated VIS migrated rapidly into the scratch and filled it nearly completely (Figure S12, Supporting

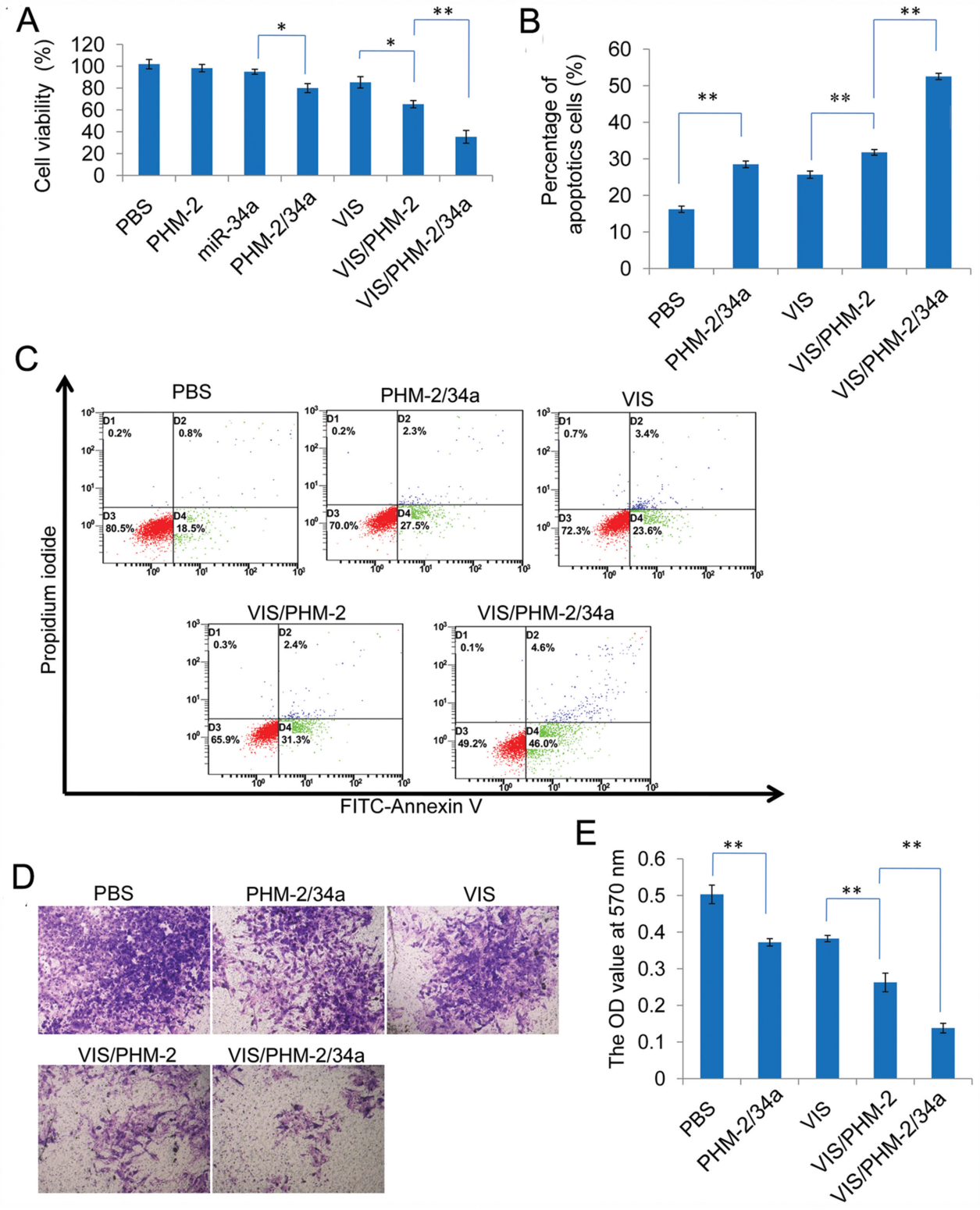

Figure 4. Antitumor effects of VIS/PHM-2/34a on B16F10-CD44$^+$ cells in vitro. A) Cell viability assay of B16F10-CD44$^+$ cells treated with different formulations ($n = 3$, mean ± SD). *$p < 0.05$, **$p < 0.01$. B,C) Apoptosis of B16F10-CD44$^+$ cells induced by different formulations of VIS and miR-34a. After 72 h incubation, cells were harvested, stained with FITC-Annexin V and propidium iodide (PI), and analyzed by flow cytometry. B) The proportion of apoptotic cells in each sample ($n = 3$, mean ± SD; **$p < 0.01$). C) Representative dot plot for each sample. D,E) Invasion assay of B16F10-CD44$^+$ cells treated with different formulation of VIS and miR-34a. Cells that invaded through the pores were stained with crystal violet and analyzed D) qualitatively by light microscopy and E) quantitatively by measuring optical density at 570 nm ($n = 3$, mean ± SD; **$p < 0.01$).

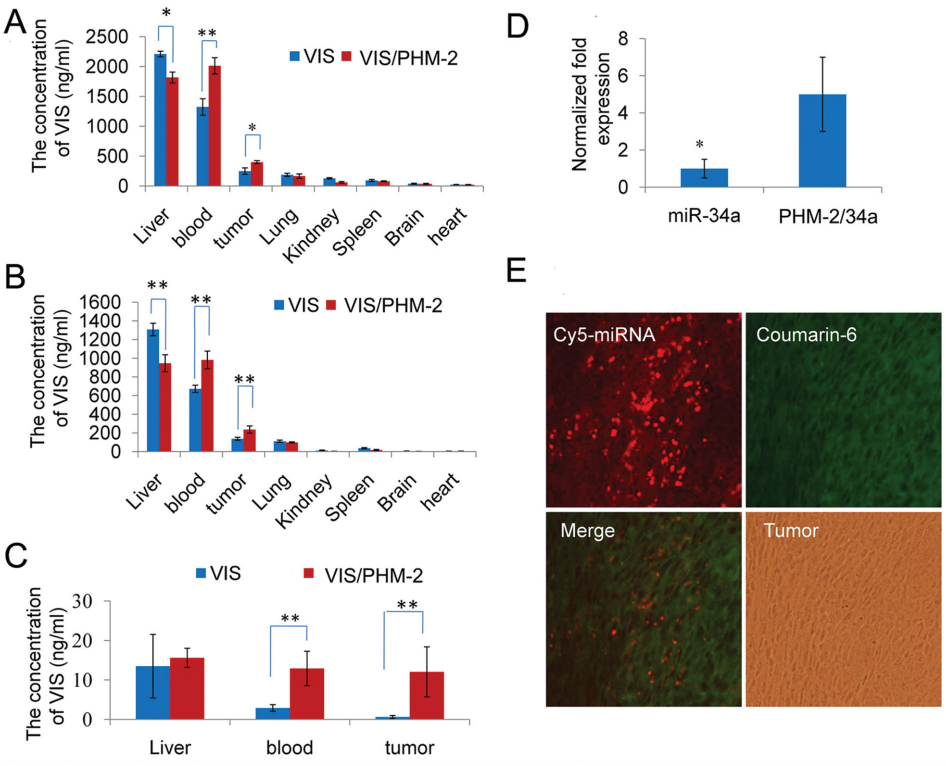

Figure 5. Co-delivery of miR-34a and VIS into tumors in vivo by VIS/PHM-2/34a. A–C) Tissue distribution of VIS in mice bearing B16F10-CD44$^+$ xenograft tumors. Tissue was sampled at different times after intravenous injection with unencapsulated VIS or VIS/PHM-2/34a at a dose of 25 mg VIS per kg ($n = 6$, mean ± SD): A) 0.5 h, B) 2 h, and C) 8 h. *$p < 0.05$, **$p < 0.01$. D) Distribution of miR-34a in tumors of mice bearing B16F10-CD44$^+$ xenografts at 2 h after intravenous administration of miR-34a and VIS/PHM-2/34a ($n = 5$, mean ± SD). *$p < 0.05$, **$p < 0.01$ at a dose of 2.5 mg miR-34a per kg. E) Fluorescence micrographs of tumor tissue sections taken from mice bearing B16F10-CD44$^+$ xenografts at 2 h after intravenous injection of coumarin-6/PHM-2/Cy5-miRNA at a dose of 2 mg coumarin-6 per kg and 2.5 mg Cy5-miRNA per kg. Green fluorescence shows the location of coumarin-6; red fluorescence, Cy5-miRNA.

Information), whereas wound healing occurred much more slowly in cultures preincubated with PHM-2/34a, VIS/PHM-2, or VIS/PHM-2/34a. VIS/PHM-2/34a inhibited migration to a much greater extent than either of the other two formulations.

2.6. Co-delivery of miR-34a and VIS into Tumor Cells by VIS/PHM-2/34a In Vivo

To examine how well PHM-2 can target drugs to melanoma tumors and efficiently co-deliver VIS and miR-34a, we injected VIS/PHM-2/34a intravenously into mice bearing B16F10-CD44$^+$ melanoma xenografts and examined drug accumulation in the tumor. Serum levels of VIS were significantly higher in animals injected with VIS/PHM-2/34a than in animals injected with unencapsulated VIS at given time points (**Figure 5**A–C). Similarly, VIS levels in the tumor were significantly higher in animals injected with VIS/PHM-2/34a than in animals injected with unencapsulated VIS at predetermined time points examined. By 8 h after injection, VIS levels in the tumor were nearly tenfold higher in animals injected with VIS/PHM-2/34a than in VIS-injected ones. The results were equally promising for miR-34a: at only 2 h after injection, levels of the miR-34a in tumor were fivefold higher in animals injected with VIS/PHM-2/34a than in animals injected with unencapsulated miR-34a (Figure 5D). These biodistribution studies clearly indicate that PHM-2 can significantly enhance tumor accumulation of VIS and miR-34a in vivo.

To gain higher-resolution data on the biodistribution of the co-delivered drugs, we incorporated coumarin-6 and Cy5 labeled miRNA into the PHM-2, prepared the corresponding coumarin/PHM-2/Cy5-miRNA micelles, and injected them into mice. Under the fluorescence microscope, frozen tumor sections showed abundant signal from coumarin-6 and Cy5-miRNA within the tumor (Figure 5E), suggesting efficient intracellular delivery of both molecules into tumor cells.

2.7. VIS/PHM-2/34a Exhibits the Highest Antitumor Efficacy In Vivo

Antitumor efficacy of VIS/PHM-2/34a was studied in mice bearing B16F10-CD44$^+$ melanoma xenografts. Tumors grew rapidly in mice treated with saline, whereas they grew substantially more slowly in the animals treated with unencapsulated VIS, PHM-2/34a, VIS/PHM-2, or VIS/PHM-2/34a (**Figure 6**A). The latter three groups of mice also lived substantially longer than the saline group (Figure 6B). Tumor inhibition rate was 32% for unencapsulated VIS, which was much lower than the rates of 51.5% for VIS/PHM-2 and 65% for PHM-2/34a. VIS/PHM-2/34a was associated with the highest tumor inhibition rate

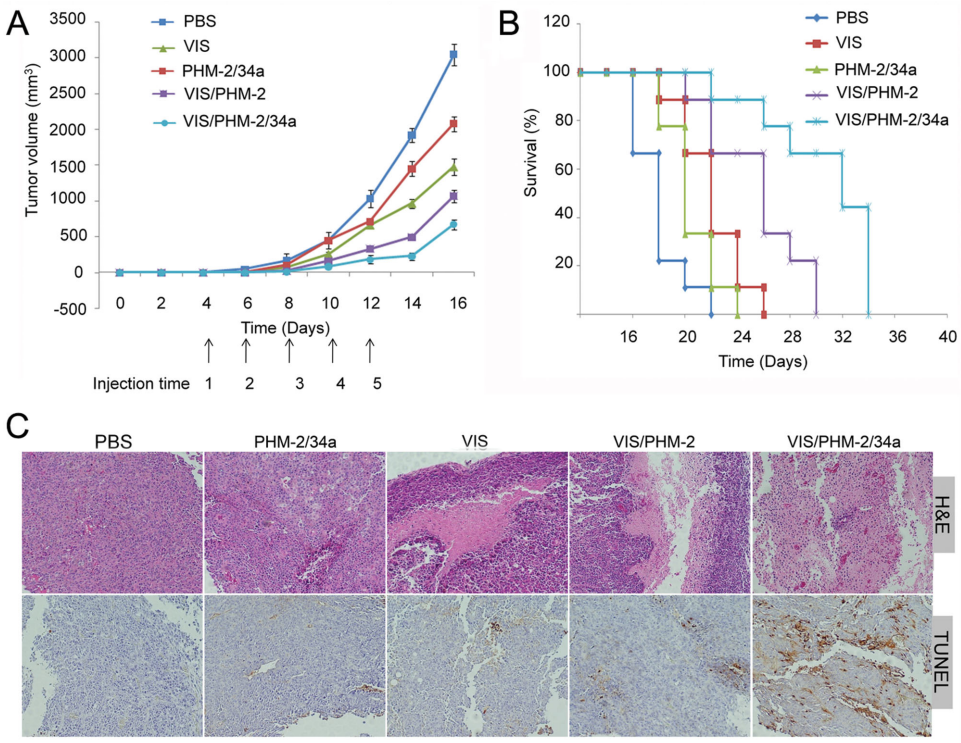

Figure 6. Antitumor effects of VIS/PHM-2/34a in mice bearing B16F10-CD44$^+$ xenografts. The doses of VIS and miR-34a were 25 mg kg^{-1} and 2.5 mg kg^{-1} per injection on days 4, 6, 8, 10, and 12 after initial tumor cell injection ($n = 6$). A) Growth curves of tumors in mice bearing B16F10-CD44$^+$ xenografts receiving various treatments ($n = 6$, mean ± SD). B) Survival analysis of mice bearing B16F10-CD44$^+$ tumors ($n = 10$). C) Hematoxylin-eosin staining and TUNEL staining of tumor tissue from mice bearing B16F10-CD44$^+$ xenografts following various treatments. Tumor tissue was collected 24 h after the last treatment injection.

(80%), which was significantly higher than that observed for the other treatments ($p < 0.01$). In fact, complete tumor regression was observed in two of the six animals treated with VIS/PHM-2/34a, but not in any of the other treatment or control groups.

The ability of the co-delivered drugs to induce apoptosis in xenograft tumors was analyzed directly using terminal deoxynucleotidyl transferase-mediated dUTP nick end-labeling (TUNEL), while their ability to induce necrosis was assessed using hematoxylin and eosin (H&E). Tumors from animals treated with unencapsulated VIS, PHM-2/34a, VIS/PHM-2, or VIS/PHM-2/34a showed a higher proportion of TUNEL-positive cells than tumors from animals treated with PBS (Figure 6C). VIS/PHM-2/34a was associated with the largest proportion of TUNEL-positive tumor cells among all the groups. H&E staining revealed extensive histopathology and necrosis in most of the tumor area in animals treated with unencapsulated VIS, PHM-2/34a, VIS/PHM-2, or VIS/PHM-2/34a, while little or no such histopathology was detected in tumors from animals treated with PBS (Figure 6C). VIS/PHM-2/34a was associated with greater histopathology and necrosis than the other treatments.

2.8. VIS/PHM-2/34a Inhibits Melanoma Growth by Inhibiting Hh Signaling and Synergistically Attenuates CD44 Expression

The present study relied on B16F10-CD44$^+$ cells as a model of aggressive or metastatic melanoma. CD44 is a ubiquitous multistructural and multifunctional cell surface glycoprotein involved in cell migration, self-renewal, drug resistance, and apoptosis resistance.[20] It is an indicator of tumors and metastasis in malignant diseases.[19b] In addition, it was found that CD44 overexpressed in melanoma and associated with the melanoma growth, invasion, and metastasis.[19a,21] In our previous research, it was shown that the sorted B16F10-CD44$^+$ cell subsets displayed cancer stem cell (CSC) characteristics (sphere, colony forming potential, expression of other CSC-related markers, and tumorigenic ability when transplanted in mouse xenograft model) other than B16F10-CD44$^-$ cells.[15a] Although the existence of CSCs remains a topic of intense debate, the results of our previous study clearly demonstrated that such subpopulation of CD44$^+$ cells in B16F10 cell line is much more malignant than the CD44$^-$ populations and elimination of the CD44$^+$ melanoma cells displaying CSC characteristics is crucial for the successful treatment of melanoma. Therefore we chose to conduct the present studies on B16F10-CD44$^+$ cells rather than on bulk B16F10 cells.

We designed the VIS/PHM-2/34a co-delivery system in order to inhibit melanoma growth and metastasis through two pathways: miR-34a was intended to reduce CD44 expression, as we discovered in previous work,[15a] while VIS was intended to inhibit Hh signaling.[22] To explore the mechanism of synergistic anticancer effect, it is necessary to investigate the effect of VIS/PHM-2/34a on the CD44 expression and Hh signaling in B16F10-CD44$^+$ cells. We treated B16F10-CD44$^+$ cells with

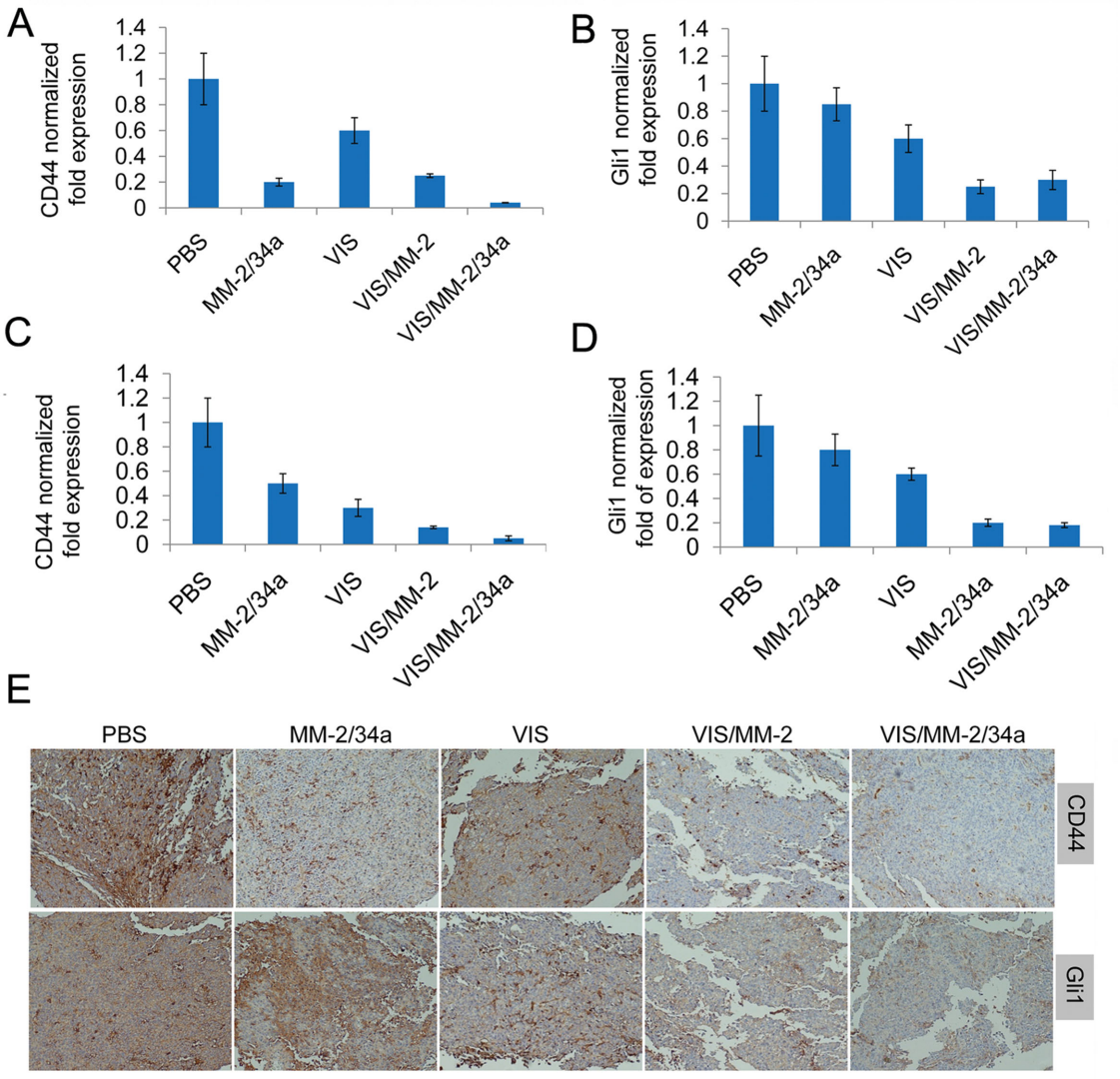

Figure 7. Effect of VIS/PHM-2/34a on CD44 and Gli1 expression in B16F10-CD44$^+$ cells in vitro and in vivo. Real-time PCR analysis of A) CD44 and B) Gli1 expression in cells treated with various formulations. Real-time PCR analysis of C) CD44 and D) Gli1 expression in tumors from mice bearing B16F10-CD44$^+$ xenografts after treatment with various formulations. E) Representative micrographs showing CD44 and Gli1 immunohistochemistry in tumors from mice bearing B16F10-CD44$^+$ xenografts after treatment with various formulations.

unencapsulated VIS, VIS/PHM-2/34a, or other PHM formulations, and then measured levels of CD44 mRNAs. In addition, the mRNA levels of glioma-associated oncogene homolog 1 (Gli1), a strong constitutive transcriptional activator in Hh pathway,[23] were also measured to investigate the activity of Hh signaling in treated B16F10-CD44$^+$ cells. As shown in the **Figure 7**A,B, all treatments reduced expression of CD44 or Gli1 mRNAs below the levels in cells treated with PBS. Cells treated with VIS/PHM-2/34a showed the strong simultaneously inhibition of CD44 and Gli1. Moreover, cells treated with VIS/PHM-2/34a showed much lower expression of CD44 than cells treated with PHM-2/34a or VIS/PHM-2, raising the possibility that co-delivery of VIS and miR-34a synergistically attenuates CD44 expression in B16F10-CD44$^+$ cells.

To further investigate in vivo whether VIS/PHM-2/34a could inhibit the CD44 expression and Hh signaling in B16F10-CD44$^+$ cells, we treated mice bearing B16F10-CD44$^+$ melanoma xenograft tumors with VIS/PHM-2/34a or other formulations and determined CD44 and Gli1 expression in the tumors using real-time PCR and immunohistochemistry (Figure 7C–E). Levels of CD44 mRNA were much lower in the animals treated with VIS/PHM-2/34a than in animals treated with PHM-2/34a or VIS/PHM-2 (Figure 7C). These results confirm the in vitro suggestion of synergistic downregulation of CD44 expression in B16F10-CD44$^+$ cells. In contrast, VIS/PHM-2/34a did not show such potentially synergistic inhibition of Gli1 relative to PHM-2/34a or VIS/PHM-2, just as in the in vitro experiments (Figure 7D). Immunohistochemistry against CD44 and Gli1 showed similar results as the real-time PCR experiments in vitro and in vivo (Figure 7E).

Interestingly, VIS not only inhibited the cellular levels of Gli1 but also notably downregulated CD44 expression (Figure 7A,B).

These suggested that VIS, in addition to being a known Hh pathway inhibitor, may also have a role in the suppression of CD44 expression in B16F10-CD44$^+$ cells. To test this possibility directly, we treated B16F10-CD44$^+$ cells using other Hh pathway inhibitors and examined the effects on CD44 expression. All the Hh pathway inhibitors reduced CD44 expression in a dose-dependent manner (Figure S13, Supporting Information). These results provide what we believe to be the first direct evidence about the role of Hh signaling pathway in modulating CD44 expression in B16F10-CD44$^+$ cells. They further suggest that Hh signaling might be an upstream regulator of CD44 expression in melanoma cells. In many tumor types, ligand-dependent activation of Hh signaling is potentiated through crosstalk with other critical molecular signaling pathways, such as RAS/RAF/MEK/ERK, PI3K/AKT/mTOR, EGFR, and Notch pathway.[24] Based on the observed crosstalk between Hh and other signaling pathways, combinations of Hh inhibitors with inhibitors of other key pathways are now being investigated in rational, mechanism-based preclinical and clinical studies in diverse tumor types.[24b,25] Some of these studies have demonstrated synergistic anticancer effect in a wide array of tumors, suggesting that understanding the underlying correlation between the Hh pathway and other signaling pathways will facilitate the design of rational combination therapies to enhance the anticancer effect of Hh pathway inhibitors. Therefore, the potential correlation between the Hh signaling and CD44 expression is worth further studying and could help us to rationally design novel combination strategy based on Hh inhibitors and other anticancer agents.

3. Conclusions

In this study, we report a successful application of PHM as a novel nanocarrier system for co-delivery of small molecule and nucleic acid drugs. Through rational design, PHMs were well tailored with different proportions of cationic segments. The systematic study helps elucidate the impact of the cationic segment proportions on the in vivo fate of PHMs. Near neutral PHMs containing a low concentration of PCL-PEI (PHM-2) achieved high tumor distribution and well biocompatibility. Afterward, miR-34a and VIS were co-encapsulated into PHM-2 which showed synergistic anticancer efficacy in B16F10-CD44$^+$ cells both in vitro and in vivo. In addition, Hh signaling was found to be an upstream regulator of CD44 expression in melanoma cells, providing the first evidence of correlation between the Hh pathway and CD44 expression in melanoma cells. In summary, our study presented a potential combination strategy to treat melanoma, as well as a novel co-delivery platform that can be easily tailored to achieve high loading of therapeutics, intracellular delivery, extended serum half-life, tumor targeting, and low toxicity.

4. Experimental Section

Preparation and Characterization of VIS/PHM-2/miR-34a: VIS was encapsulated into PHM-2 to obtain VIS/PHM-2, which was incubated with miR-34a to yield VIS/PHM-2/34a. The detailed steps were as follows. VIS powder (0.5 mg), 25 mg of PCL-PEG, and 1.25 mg of PCL-PEG were dissolved in 2 mL of tetrahydrofuran. This solution was slowly added to 20 mL of pure water and stirred at moderate speed at room temperature for 20 min. The organic solvents were removed by rotary vacuum evaporation at 37 °C, yielding VIS/PHM-2. A solution of miR-34a in RNase-free water was mixed with VIS/PHM-2 at an N:P ratio of 10:1 by gentle pipetting, then the mixture was incubated at room temperature for 30 min to obtain VIS/PHM-2/34a. Dynamic light scattering was used to measure particle size and zeta potential of VIS/PHM-2/34a (Zetasizer Nano ZS90, Malvern, UK). The morphology of VIS/PHM-2 and VIS/PHM-2/34a after staining with 0.1% phosphotungstic acid was examined by transmission electron microscopy (H-600, Hitachi, Japan). Drug-loading (DL%) and encapsulation efficiency (EE%) of VIS and miR-34a in VIS/PHM-2/34a were determined using ultrafiltration method (300 kD, 3000 g, 30 min). FITC-labeled miRNA was used to enable fluorometric measurements of miRNA concentration. The total amount of FITC-labeled miRNA was determined by fluorescence spectrophotometry. VIS/PHM-2/34a was diluted with methanol and subsequently analyzed by LC-MS to determine the total amount of VIS. Briefly, VIS/PHM-2/34a was ultrafiltered, and the filtrate was collected to analyze the amount of free VIS by LC-MS and the amount of FITC-labeled miRNA by fluorescence spectrophotometry. DL% and EE% were calculated using Equation (1) and Equation (2), respectively

$$\mathrm{EE\%} = \frac{\text{Weight of drug in PHM}}{\text{Weight of the drug added}} \times 100\% \quad (1)$$

$$\mathrm{DL\%} = \frac{\text{Weight of drug in PHM}}{\text{Total weight of PHM}} \times 100\% \quad (2)$$

The in vitro release of VIS from VIS/PHM-2/34a was investigated using the dialysis method. Initially, 1 mL of VIS/PHM-2, VIS/PHM-2/34a, or free VIS solution was placed into dialysis bags with a molecular weight cutoff of 8–12 kDa (Millipore, USA). Then the dialysis bags were immersed in 250 mL PBS (pH 7.4) containing 0.2% (v/v) Tween 80 and incubated at 37 °C with constant shaking at 100 rpm. At specific time points, 1 mL of release medium was removed for analysis and replaced with 1 mL of fresh medium. The samples of release medium were diluted with methanol, and the concentration of released VIS was determined using a validated LC-MS method. DTA was performed in a DTA analyzer (Netzsch DTA 200 PC, Germany). Dried samples of free VIS, empty PHM-2, and VIS/PHM-2 were sealed in the aluminum crimp cell and heated from 0 to 300 °C at 10 °C per minute under a nitrogen atmosphere. To investigate the stability of miR-34a in the presence of serum, free miR-34a (100 μL, 1 μg) or Vis/PHM/miR-34a containing 1 μg of miR-34a was incubated at 37 °C for 6 h with 100 μL of serum from C57BL/6 mice or 10% FBS. Then miR-34a was extracted from the solution using an RNA isolation kit (TianGen, Beijing, China), and levels of remaining miR-34a were determined by real-time PCR in terms of the threshold cycle (C_t) value.[26]

Cell Viability and Apoptosis Assay: First, CD44 positive B16F10 cells were sorted by using antimouse CD44 FITC antibody (eBioscience, USA). Then the mean purity of CD44-enriched cells, determined by flow cytometry using the Cytomics FC500 flow cytometer (Beckman Coulter, Miami, FL), was 96.4%. Proliferation of drug-treated B16F10-CD44$^+$cells was determined using the Cell Counting Kit-8 (Beyotime, China). B16F10-CD44$^+$ cells were plated in 96-well plates and incubated for 24 h. Then cells were treated in triplicate with various formulations for 4 h, after which the medium was replaced with fresh complete medium and the cells were cultured another 72 h. Afterward the medium was replaced with 100 μL of fresh medium containing 10% of CCK-8 solution. The cells were incubated another 1.5 h, and medium absorbance at 450 nm was measured using a Varioskan Flash microplate reader (Thermo, USA). To examine apoptosis, B16F10-CD44$^+$ cells were incubated in 12-well plates for 24 h. Then cells were treated with various formulations for 4 h, after which they were given fresh complete medium and cultured for another 72 h. Finally, cells were fixed in 4% paraformaldehyde

for 5 min and stained with DAPI.[15a,27] Extent of cell apoptosis was determined by assessing nuclear morphology under a fluorescence microscope operating at an excitation wavelength of 358 nm and an emission wavelength of 461 nm. Proportions of apoptotic cells were also quantified by flow cytometry after double staining with FITC-Annexin V and PI using a cell apoptotic analysis kit (BD, USA) according to the manufacturer's instructions.

In Vitro Migration and Invasion Assays: For invasion assays, drug-treated B16F10-CD44$^+$ cells were seeded at 2×10^4 cells per well in the upper chamber of a transwell with a Matrigel-coated membrane (24-well insert, 8 μm pore size). Cells in the upper chamber were cultured in medium without serum. Medium containing 20% serum was added to the lower chamber; the serum acted as a chemo attractant. After 72 h incubation, the plate was stained with crystal violet and cell invasion through the pores was observed by light microscopy and quantitated by measuring absorption at 570 nm on a Varioskan Flash microplate reader.

B16F10-CD44$^+$ Subcutaneous Xenograft Model: Female C57BL/6 mice aged 5–7 weeks were purchased from the Laboratory Animal Center of Sichuan University (Chengdu, China). All animal experiments were approved by the Institutional Animal Care and Ethics Committee of Sichuan University. A suspension of B16F10-CD44$^+$ cells (0.1 mL, 1×10^5 cells) was injected subcutaneously into the right flank of C57BL/6 mice to induce growth of subcutaneous tumor xenografts.

Biodistribution of VIS/PHM-2/miR-34a: In vivo imaging and biodistribution experiments were performed ≈14 days after tumor cell injection, by which time tumors had grown to ≈1 cm in diameter. At that time, free VIS solution or VIS/PHM-2/miR-34a was administered to B16F10-CD44$^+$ tumor-bearing mice via the tail vein at a dose of 10 mg VIS per kg. At 0.5, 2, and 8 h after injection, five mice were sacrificed and their blood and several tissues were collected, including the heart, lung, liver, kidney, spleen, brain, and tumor. Plasma samples were obtained by centrifuging blood at 4000 *g* for 4 min. Tissue samples were accurately weighed, homogenized, and extracted with three volumes of 0.9% NaCl solution to give a concentration of 250 mg mL^{-1}. VIS was extracted by mixing 100 μL of tissue or plasma with 500 μL of acetonitrile. The mixtures were vortexed for 15 min and then centrifuged at 4000 *g* for 10 min. An aliquot of clear supernatant (1 μL) was injected into the LC-MS system. To determine the concentration of miR-34a in tumor tissue, free miR-34a solution or VIS/PHM-2/34a was administered to B16F10-CD44$^+$ tumor-bearing mice via the tail vein at a dose of 2.5 mg miR-34a per kg. At 2 h after injection, five mice from each group were sacrificed and tumor tissue was collected. Levels of miR-34a in tumor were determined using real-time PCR (iCycler iQ 5, Bio-Rad, USA). To visualize co-delivery of VIS and miR-34a from VIS/PHM-2/miR-34a into tumor cells, a dual-labeled delivery system was prepared by encapsulating both coumarin-6 and Cy5-miRNA into PHM-2. The resulting coumarin-6/PHM/Cy5-miRNA was injected into tumor-bearing mice via the tail vein at a dose of 2 mg coumarin-6 per kg. At 0.5 h after injection, the tumor was excised, cryopreserved in tissue freezing medium (Leica CM 1950), then cut into cross-sections, and mounted on glass slides for fluorescence microscopy analysis (TCS SP5, Leica, Germany).

In Vivo Anticancer Efficacy: At 4 days after tumor cell injection, B16F10-CD44$^+$ tumor-bearing mice were randomly divided into five groups (six mice per group), each of which was injected intravenously with PBS, PHM/34a, unencapsulated VIS, VIS/PHM, or VIS/PHM/34a on days 4, 6, 8, 10, and 12 after initial tumor cell injection. Treatments were injected each time at a dose of 25 mg VIS per kg and 2.5 mg miR-34a per kg. Tumor growth and body weight were monitored, and tumor volume was calculated using the formula $(L \times W^2/2)$, where W refers to the smaller diameter and L to the larger. On day 16, animals were sacrificed and tumors were collected for ex vivo histological analysis. The tumor inhibition ratio (TIR) was calculated using the equation $\mathrm{TIR}(\%) = (1 - V_t/V_c) \times 100\%$, where V_t and V_c refer to the average tumor volume on day 16 in the treatment and control groups, respectively. Levels of CD44 and Gli1 mRNA in tumor were analyzed using real-time PCR. In separate experiments to determine survival, B16F10-CD44$^+$ tumor-bearing mice were treated as above and dates of death were recorded. Survival data between treatment groups were compared using SPSS 19.0 (IBM, Chicago, IL, USA).

Statistical Analysis: All quantitative data were expressed as mean ± SD from triplicate measurements, unless otherwise noted. Differences between treatment groups were assessed for significance using single-factor analysis of variance, followed by Student's *t*-test. The threshold for significance was $p < 0.05$.

Supporting Information

Supporting Information is available from the Wiley Online Library or from the author.

Acknowledgements

This project was supported by the National Natural Science Foundation of China (Grant Nos. 81173011 and 81422044) and the National Science & Technology Major Project of China (Grant No. 2012ZX09304004).

Received: July 27, 2015
Revised: September 21, 2015
Published online: November 10, 2015

[1] a) G. Feng, H. Chen, J. Li, Q. Huang, M. J. Gupte, H. Liu, Y. Song, Z. Ge, *Biomaterials* **2015**, *52*, 1; b) A. Bouchie, *Nat. Biotechnol.* **2013**, *31*, 577; c) A. Sato, S. W. Choi, M. Hirai, A. Yamayoshi, R. Moriyama, T. Yamano, M. Takagi, A. Kano, A. Shimamoto, A. Maruyama, *J. Controlled Release* **2007**, *122*, 209.
[2] a) L. Zhu, P. Kate, V. P. Torchilin, *ACS Nano* **2012**, *6*, 3491; b) J. Li, Y. Wang, Y. Zhu, D. Oupicky, *J. Controlled Release* **2013**, *172*, 589.
[3] a) T. C. Chou, *Cancer Res.* **2010**, *70*, 440; b) X. Dai, C. Tan, *Adv. Drug Delivery Rev.* **2015**, *81*, 184.
[4] L. Ma, M. Kohli, A. Smith, *ACS Nano* **2013**, *7*, 9518.
[5] a) C. Zheng, M. Zheng, P. Gong, J. Deng, H. Yi, P. Zhang, Y. Zhang, P. Liu, Y. Ma, L. Cai, *Biomaterials* **2013**, *34*, 3431; b) T. M. Sun, J. Z. Du, Y. D. Yao, C. Q. Mao, S. Dou, S. Y. Huang, P. Z. Zhang, K. W. Leong, E. W. Song, J. Wang, *ACS Nano* **2011**, *5*, 1483.
[6] C. E. Nelson, J. R. Kintzing, A. Hanna, J. M. Shannon, M. K. Gupta, C. L. Duvall, *ACS Nano* **2013**, *7*, 8870.
[7] a) C. W. Evans, M. Fitzgerald, T. D. Clemons, M. J. House, B. S. Padman, J. A. Shaw, M. Saunders, A. R. Harvey, B. Zdyrko, I. Luzinov, G. A. Silva, S. A. Dunlop, K. S. Iyer, *ACS Nano* **2011**, *5*, 8640; b) P. van de Wetering, E. E. Moret, N. M. Schuurmans-Nieuwenbroek, M. J. van Steenbergen, W. E. Hennink, *Bioconjugate Chem.* **1999**, *10*, 589.
[8] a) T. K. Endres, M. Beck-Broichsitter, O. Samsonova, T. Renette, T. H. Kissel, *Biomaterials* **2011**, *32*, 7721; b) X. Yang, J. J. Grailer, I. J. Rowland, A. Javadi, S. A. Hurley, V. Z. Matson, D. A. Steeber, S. Gong, *ACS Nano* **2010**, *4*, 6805; c) H. Yin, E. S. Lee, D. Kim, K. H. Lee, K. T. Oh, Y. H. Bae, *J. Controlled Release* **2008**, *126*, 130.
[9] a) H. X. Wang, M. H. Xiong, Y. C. Wang, J. Zhu, J. Wang, *J. Controlled Release* **2013**, *166*, 106; b) E. S. Lee, K. Na, Y. H. Bae, *J. Controlled Release* **2003**, *91*, 103; c) L. Mu, T. A. Elbayoumi, V. P. Torchilin, *Int. J. Pharm.* **2005**, *306*, 142.
[10] a) D. Velluto, S. N. Thomas, E. Simeoni, M. A. Swartz, J. A. Hubbell, *Biomaterials* **2011**, *32*, 9839; b) L. Qiu, M. Qiao, Q. Chen, C. Tian, M. Long, M. Wang, Z. Li, W. Hu, G. Li, L. Cheng, H. Hu, X. Zhao, D. Chen, *Biomaterials* **2014**, *35*, 9877.
[11] a) M. F. Delcroix, S. Laurent, G. L. Huet, C. C. Dupont-Gillain, *Acta Biomater.* **2015**, *11*, 68; b) S. Li, Q. He, T. Chen, W. Wu, K. Lang, Z. M. Li, J. Li, *Colloids Surf. B: Biointerfaces* **2014**, *123*, 486.

[12] R. V. Benjaminsen, M. A. Mattebjerg, J. R. Henriksen, S. M. Moghimi, T. L. Andresen, *Mol. Therapy* **2013**, *21*, 149.
[13] J. P. Singhal, A. R. Ray, *Biomaterials* **2002**, *23*, 1139.
[14] H. Otsuka, Y. Nagasaki, K. Kataoka, *Adv. Drug Delivery Rev.* **2003**, *55*, 403.
[15] a) S. Shi, L. Han, T. Gong, Z. Zhang, X. Sun, *Angew. Chem. Int. Ed.* **2013**, *52*, 3901; b) C. Liu, K. Kelnar, B. Liu, X. Chen, T. Calhoun-Davis, H. Li, L. Patrawala, H. Yan, C. Jeter, S. Honorio, J. F. Wiggins, A. G. Bader, R. Fagin, D. Brown, D. G. Tang, *Nat. Med.* **2011**, *17*, 211.
[16] A. Jalili, K. D. Mertz, J. Romanov, C. Wagner, F. Kalthoff, A. Stuetz, G. Pathria, M. Gschaider, G. Stingl, S. N. Wagner, *PloS one* **2013**, *8*, e69064.
[17] H. Xin, L. Chen, J. Gu, X. Ren, Z. Wei, J. Luo, Y. Chen, X. Jiang, X. Sha, X. Fang, *Int. J. Pharm.* **2010**, *402*, 238.
[18] R. Li, J. S. Eun, M. K. Lee, *Arch. Pharm. Res.* **2011**, *34*, 331.
[19] a) I. R. Hart, M. Birch, J. F. Marshall, *Cancer Metastasis Rev.* **1991**, *10*, 115; b) G. N. van Muijen, E. H. Danen, J. H. Veerkamp, D. J. Ruiter, J. Lesley, L. P. van den Heuvel, *Int. J. Cancer* **1995**, *61*, 241.
[20] V. Zawadzki, A. Perschl, M. Rosel, A. Hekele, M. Zoller, *Int. J. Cancer* **1998**, *75*, 919.
[21] a) T. Ahrens, V. Assmann, C. Fieber, C. Termeer, P. Herrlich, M. Hofmann, J. C. Simon, *J. Invest. Dermatol.* **2001**, *116*, 93; b) M. Birch, S. Mitchell, I. R. Hart, *Cancer Res.* **1991**, *51*, 6660.
[22] V. I. Alexaki, D. Javelaud, L. C. Van Kempen, K. S. Mohammad, S. Dennler, F. Luciani, K. S. Hoek, P. Juarez, J. S. Goydos, P. J. Fournier, C. Sibon, C. Bertolotto, F. Verrecchia, S. Saule, V. Delmas, R. Ballotti, L. Larue, P. Saiag, T. A. Guise, A. Mauviel, *J. Natl. Cancer Inst.* **2010**, *102*, 1148.
[23] a) R. Santini, M. C. Vinci, S. Pandolfi, J. Y. Penachioni, V. Montagnani, B. Olivito, R. Gattai, N. Pimpinelli, G. Gerlini, L. Borgognoni, B. Stecca, *Stem Cells* **2012**, *30*, 1808; b) A. Ruiz i Altaba, P. Sanchez, N. Dahmane, *Nat. Rev. Cancer* **2002**, *2*, 361.
[24] a) B. Stecca, C. Mas, V. Clement, M. Zbinden, R. Correa, V. Piguet, F. Beermann, I. A. A. Ruiz, *Proc. Natl. Acad. Sci. USA* **2007**, *104*, 5895; b) J. Brechbiel, K. Miller-Moslin, A. A. Adjei, *Cancer Treatment Rev.* **2014**, *40*, 750.
[25] I. Caro, J. A. Low, *Clin. Cancer Res.* **2010**, *16*, 3335.
[26] S. Shi, L. Han, T. Gong, Z. Zhang, X. Sun, *Angew. Chem. Int. Ed.* **2013**, *52*, 3901.
[27] S. Emanuele, M. Lauricella, D. Carlisi, B. Vassallo, A. D'Anneo, P. Di Fazio, R. Vento, G. Tesoriere, *Apoptosis* **2007**, *12*, 1327.